Boat-tail effects on the global wake dynamics of a flat-backed body with rectangular section

G. Bonnavion[a], O. Cadot[b,*]

[a]*IMSIA, ENSTA-ParisTech, CNRS, CEA, EDF, Université Paris Saclay, 828 Boulevard des Maréchaux, 91762 Palaiseau Cedex, France*
[b]*School of Engineering, University of Liverpool, L69 3BX Liverpool, UK*

Abstract

A three-dimensional body of rectangular section with a blunt trailing edge is studied for various angles of after-body boat-tailing. The Reynolds number of the flow is $\mathrm{Re} = 4.0 \times 10^5$ and the body is in the vicinity of the ground. It is found that the wake dynamics is strongly dependent on the coupling of top and bottom boat-tail angles, triggering either long-time bi-stability between two mirror static asymmetric states or an anti-symmetric periodic mode, both leading to large cross-flow force fluctuations. The transition is shown to depend on the aspect ratio of the vertical base and not on the flow orientations imposed by the coupling of angles. Within the limitation of the aspect ratio for which the static states persist and dominate the wake dynamics, as boat-tails are installed at the after-body, they generate a vertical base pressure gradient component on which the static states adapt according to the mechanism proposed by Bonnavion and Cadot (2018).

Keywords: bluff body, wake dynamics, static instability, boat-tailing,

*Corresponding author.
Email address:* `Olivier.Cadot@liverpool.ac.uk` (O. Cadot)

1. Introduction

Bluff bodies are known to experience large aerodynamics drag due to the substantial base suction produced by the rear massive flow separation (Roshko, 1993). For blunt-based bodies, it is well known that a reduction of their cross-section before the flow separation is an efficient way to achieve important drag reduction. Although this general trend applies to axisymmetric and rectangular base bodies (Mair, 1969; Wong and Mair, 1983), both involve different mechanisms. Basically, an ultimate low drag would be achieved for axisymmetric bodies with pointed shape trailing edge for which no flow separation occurs. However a complete pressure recovery leading to a zero net pressure drag is impossible due to the boundary layer growth unavoidably induced by pressure gradients and body streamlines convergence. As a result, the observed recovery never exceeds a pressure coefficient of +0.25 (Mair, 1969). The contribution of Mair (1969) shows that (i) a similar drag can be also obtained for shortened after-bodies with a boat-tail length of only 60% of the maximum body diameter, and (ii) that the drag contribution due to the boat-tail ahead the base is as large as that due to the blunt base. Compared to the basic blunt body with no boat-tailing, the additional short afterbody produces a base drag reduction of 80%. This emphasizes the importance of the boat-tail shape whose performance can be summarized as a balance between a pressure decrease produced by the curvature and a pressure increase induced by the diffuser angle. However Mair was not able to propose an optimal shape for drag reduction but, instead, pointed out qualitative

2

explanations for poor and good shapes based on potential flow theory.

The boat-tailing of blunt-based bluff bodies with rectangular base (Wong and Mair, 1983) gives similar drag reduction as for axisymmetric bodies when the four sides are chamfered. If the four chamfers are not adapted to homogenize the pressure distribution over the base perimeter (as for the axisymmetric case) then three-dimensional separation will produce longitudinal vortices at each corner responsible for additional induced drag (Wong and Mair, 1983). For an Ahmed body with ground proximity, Han et al. (1992) computed an optimized after-body producing 50% of total drag reduction. This boat-tail shape avoided longitudinal vortices with angles of about 20° for top and side chamfers, and 10° for the bottom chamfer over a total after-body length equal to the body height.

Much smaller modification of blunt-based bluff bodies also has substantial impact on drag. Short tapers of no more than 15% of the body height can achieve about 5% drag reduction when implemented only at the upper part of the base with an angle of 12° (Littlewood and Passmore, 2010). Such small size chamfers whose optimal angles are smaller than those of Mair (1969) and Wong and Mair (1983) provide evidence of the flow orientation at separation. In the case of a blunt-based bluff body with top and bottom tapers only, a parabolic dependency of the drag with taper angle is reported by Grandemange et al. (2013c), Grandemange et al. (2015) and Perry et al. (2016). In these works, the optimal angles for low drag are a compromise between beneficial after-body bluffness reduction due to the flow orientation and drag induced by the three-dimensional separation at the boat-tail corners (Grandemange et al., 2013c).

The goal of the present work is to study how boat-tailing influences the y-instability observed in the wake of square-back after-bodies (Grandemange et al., 2013b). This global instability is responsible for long-time bi-stable dynamics (Grandemange et al., 2013b; Volpe et al., 2015) produced by the random switching between two static mirror states breaking the reflectional symmetry (thus defining the so-called y-instability). The y-instability originates from a steady wake instability at the first bifurcation (Grandemange et al., 2012; Evstafyeva et al., 2017) of the laminar flow. Recent studies of sensitivity of these states to either steady external disturbances (Grandemange et al., 2014; Barros et al., 2017) or body inclination (Bonnavion and Cadot, 2018) have shown the importance of geometrical details on their dynamics. To the authors' knowledge, the only few papers of square-back body boat-tailing acknowledging the y-instability concern small chamfers (Grandemange et al., 2015; Perry et al., 2016; Pavia et al., 2016). Perry et al. (2016) noticed that top and bottom chamfers increase the switching frequency between the two mirror states from that observed with the square-back geometry. Those authors also report that the direction of the wake asymmetry and the top and bottom shear layers emanating from the body are actually controlled by the taper angles. These two layers are getting closer to one each other which leads to a shorter recirculation area and, according to the latest study, to a "less bi-stable" wake, *i.e.* a decrease in the magnitude of the fluctuations. This is accompanied by a reduction of the overall fluctuation level at the base, in particular near the taper associated with the larger angle, for which a decrease by nearly a factor of two can be observed.

In the present work, the strategy is to progressively modify the square-

back geometry with increasing boat-tail angles and to assess the asymmetric state properties, such as their strength, asymmetry orientation and dynamics, using the measurements of the instantaneous base pressure gradient and the cross-flow force. The paper is organized as follows. The experimental set-up is described in § 2. Results in § 3 are split into three parts: § 3.1 shows evidence of a transition between two global wake instabilities as the boat-tailing angles are increased, § 3.2 investigates how the boat-tailing influences the wake asymmetry, and § 3.3 assesses the effect on both drag and base suction. Finally, a discussion in § 4 followed by the conclusion in § 5 ends the paper.

2. Experimental setup

2.1. Wind-tunnel and model

Figure 1 provides schematic representations of the set-up. Experiments are carried out in the model-scale wind tunnel of the GIE-S2A dedicated to automotive aerodynamics. This facility is a 3/4-open jet closed-loop tunnel regulated at $T_\infty = 291 \pm 0.5$ K with a cross-section of $S_w = 3.84$ m^2 and a $9.3 \times 6.6 \times 4.15$ m plenum where the model is placed. The flow angular deviation is lower than 0.25% and the free-stream turbulence intensity lower than 0.4%. The free-stream velocity accuracy is close to 0.5% and set at $U_\infty = 20$ m.s^{-1}. The boundary layer is controlled by suction so that the incoming velocity profile presents a 3 mm displacement thickness 1.4 m upstream the centre of the model. A sketch of the plenum facility is provided in Evrard et al. (2016).
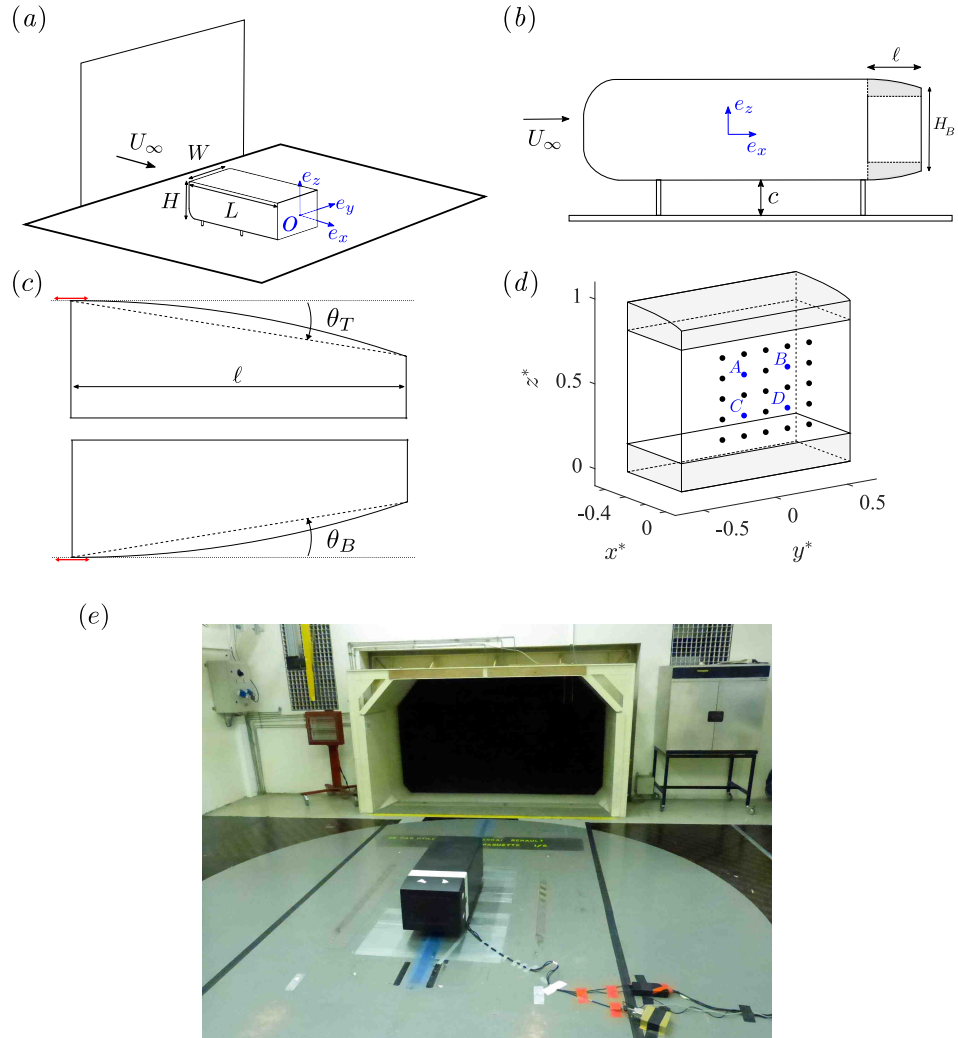
Figure 1: Experimental set-up. (a) Schematic view of the model in the wind tunnel and (b) side view of the model. The interchangeable components (boat-tails) are indicated with the dashed lines at the rear of the body in (b) and colored in grey. (c) Top and bottom boat-tail parts of length ℓ and chord angles θ_T, θ_B. (d) Locations of the pressure taps depicted as filled circles. Taps A, B, C, D are used for gradient calculations in equations (3) and (4). (e) shows a picture of the facility, with the Ahmed body viewed from behind.

The model used for experiments is the flat-backed Ahmed body represented in figure 1(a), whose characteristic dimensions are $H \times W \times L = 0.298 \times 0.350 \times 0.994$ m. The base aspect ratio in the square-back configuration equals that of the rectangular body section and is $W^* = W/H = 1.174$. With boat-tailing, the body base is characterized by the height of the vertical part denoted H_B and represented in figure 1(b). In this case, the base aspect ratio becomes $\kappa = W/H_B$. The model's ground clearance defined as the normal distance from the body to the ground and indicated in figure 1(b) is $c = 0.168H$ and the Reynolds number is $\text{Re} = U_\infty H/\nu \simeq 4.0 \times 10^5$, where ν is the air kinematic viscosity. Throughout, dimensionless quantities denoted with a superscript * are based on the body's height H and on the free-stream velocity U_∞; as a result, the dimensionless time unit is $t^* = t \cdot U_\infty/H$ and dimensionless frequencies, or equivalently Strouhal numbers, are $f^* = \text{St} = f \cdot H/U_\infty$.

The shape of the after-body is modified up to a distance $\ell = 0.537H$ upstream from the base owing to the two interchangeable components shown in grey in figure 1(b, d). The boat-tails consist of arcs of circle with horizontal tangents upstream with the body (red segment in figure 1c). The characteristic angles, θ_B for the bottom and θ_T for the top one, are defined by the chord angle as shown in figure 1(c) and take the values $\{0°, 5°, 7.5°, 10°, 12.5°\}$, thus leading to 25 possible after-body configurations.

The origin O of the coordinate system is set at the base, in the mid-height plane and on the symmetry plane. The $\mathbf{e}_x$ axis is normal to the base pointing downstream and $\mathbf{e}_z$ is upwards oriented. $\mathbf{e}_y$ is chosen accordingly to obtain the right-handed orthonormal coordinate system represented in figure 1(a, b).

2.2. Measurements of wall pressure and aerodynamic force

The model is instrumented with $n = 25$ pressure taps identified by the dots in figure 1(d) connected to a Scanivalve ZOC33b (20" H2O) pressure scanner controlled by a GreenLake Engineering SmartZOC200 electronics and a custom LabVIEW acquisition suite. The sampling frequency is 100 Hz. However, the actual cut-off frequency of the pressure measurements due to the vinyl tubing length connecting the pressure tap to the scanner is approximately 20 Hz. Nonetheless, it is sufficient to capture the long-time dynamics of the wake that occur at lower frequencies than a few hertz (Grandemange et al., 2013b). The pressure scanner actually gives the differential pressure $p - p_\infty$, where the static pressure p_∞ is obtained from the upstream section of the facility. This differential pressure is expressed as the dimensionless pressure coefficient c_p, where ρ is the air density:

$$c_p = \frac{p - p_\infty}{\frac{1}{2}\, \rho\, U_\infty^2}. \tag{1}$$

The instantaneous base suction coefficient c_b is assessed from the n pressure taps of the base:

$$c_b = -\iint_{H_B \times W} c_p ds \approx -\frac{1}{n} \sum_{i=1}^{n} c_p(y_i^*, z_i^*). \tag{2}$$

A base pressure gradient $\mathbf{g}^*$ is computed using the taps in blue color and indicated as A, B, C, D in figure 1(d). The two Cartesian component are computed as:

$$g_y^* = \frac{1}{2} \times \left[\frac{c_p(y_B^*, z_B^*) - c_p(y_A^*, z_A^*)}{y_B^* - y_A^*} + \frac{c_p(y_D^*, z_D^*) - c_p(y_C^*, z_C^*)}{y_D^* - y_C^*} \right] \tag{3}$$

and:

$$g_z^* = \frac{1}{2} \times \left[\frac{c_p(y_A^*, z_A^*) - c_p(y_C^*, z_C^*)}{z_A^* - z_C^*} + \frac{c_p(y_B^*, z_B^*) - c_p(y_D^*, z_D^*)}{z_B^* - z_D^*} \right] \tag{4}$$

8

These two quantities are used to define the complex base pressure gradient $\mathbf{g}^* = g_y^* + i g_z^*$. We use both the Cartesian and polar form of $\mathbf{g}^*$ respectively denoted (g_y^*, g_z^*), referred to as horizontal and vertical gradient components, and (g_r^*, φ), referred to as strength and orientation.

Force measurements are recorded at the sampling frequency of 10 Hz with a six-components force balance provided by Schencker GmbH and located below the wind tunnel floor. The unsteady forces f_x, f_y and f_z, corresponding respectively to drag, side force and lift are made non-dimensional into the coefficients:

$$c_i = \frac{f_i}{\frac{1}{2}\, \rho\, S\, U_\infty^2}, \quad i = \{x, y, z\}, \tag{5}$$

where S is the projected frontal area of the body.

Before each set of experiments, a no-wind acquisition is performed whose averaged value is subtracted from the actual measurements to correct any offset.

Pressure distributions $c_p(y, z, t)$ and force coefficients $c_i(t)$ are simultaneously recorded during $t = 180$ s (equivalently, $t^* = 12080$). Density power spectra are averaged from spectra computed in windows of 2048 points (20.48 s), thus leading to a frequency resolution of $\delta f^* = 7.3 \times 10^{-4}$.

3. Results

3.1. Transition in the global wake instability

Top and bottom boat-tails mainly produce a lift on the model as can be seen in figure 2(a). In the square-back configuration ($\theta_B = \theta_T = 0$), the mean lift coefficient is not zero (as would have been expected by the body symmetry), but negative with $C_z = -0.119$ because of the ground proximity.

9

It is due to a blockage effect that is even amplified when the bottom angle is increased and then saturates for $\theta_B > 10°$ as shown in figure 2(a). It is likely that the extra low pressure produced by the bottom boat-tail curvature is intensified by this blockage. This intensification explains the vertical shift of all the curves in figure 2(a) having $\theta_B \neq 0°$ compared to the series $\theta_B = 0°$. Except for this ground effect, the global trend is that lift is increased (resp. decreased) when the top angle becomes larger (resp. smaller) than the bottom angle, as a consequence of the low pressures produced by the boat-tail curvatures. At the base of the body, the vertical component of the pressure gradient shown in figure 2(b) does not simply follow an opposite trend of the lift coefficient because the pressure at separation also results from a divergent flow at the boat-tail associated with a pressure increase. For large angles, this pressure increase compensates the low pressure associated with the curvature resulting in the gradient saturation and decreases at large $|\theta_B - \theta_T|$ as observed in figure 2(b).
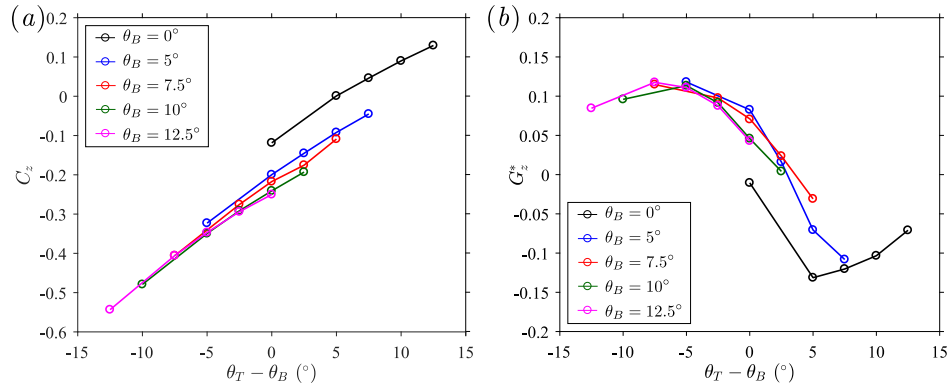

Figure 2: (a) Mean lift coefficient C_z and (b) mean vertical component of the base pressure gradient G_z^* plotted against the difference between the boat-tail angles $\theta_T - \theta_B$.

More interestingly, the mean fluctuation of both the base pressure gradient and the lift coefficient in figure 3 undergoes a large growth for approximately the same couple of the bottom/top angles, *i.e.* for $\theta_B - \theta_T \approx 0°$. The configuration of largest fluctuations are denoted $S1$, $S2$, $S3$ when they appear in the horizontal y-component for the configurations with $\theta_B = 0°, 5°, 7.5°$ in figure $3(a)$ and $P1$, $P2$ in the vertical z-component for the configurations with $\theta_B = 10°, 12.5°$ in figure $3(b)$. The large fluctuations orientated in the horizontal y-direction when the bottom boat-tail angle is $\theta_B < 10°$ are thus transferred to the vertical z-direction when $\theta_B > 10°$. The cross-flow force fluctuations (figures $3c, d$) reach their maxima for the same values as the gradients, in agreement with the gradient–cross-flow forces relationships recently derived by Bonnavion and Cadot (2018).

We then investigate the nature of both orientated fluctuations to reveal a transition between a global wake dynamics dominated by a three-dimensional steady instability and a two-dimensional periodic instability. The pressure gradient time series for the three high fluctuating cases $S1$, $S2$ and $S3$ are respectively shown in figures $4(a, b, c)$. For the square-back body in figure $4(a)$, we retrieve the long-time bi-stable dynamics described in Grandemange et al. (2013b). As the boat-tailing is applied with increasing angles from $S2$ in figure $4(b)$ to $S3$ in figure $4(c)$, the amplitude of the horizontal pressure gradient is reduced and the switching frequency between opposite gradients is increased as observed by Perry et al. (2016); this looks very similar to the stabilisation mechanism of the y-instability identified while increasing the depth of a base cavity in Evrard et al. (2016). The signature of the bi-stable dynamics is identified as low frequency power laws (Grandemange et al.,
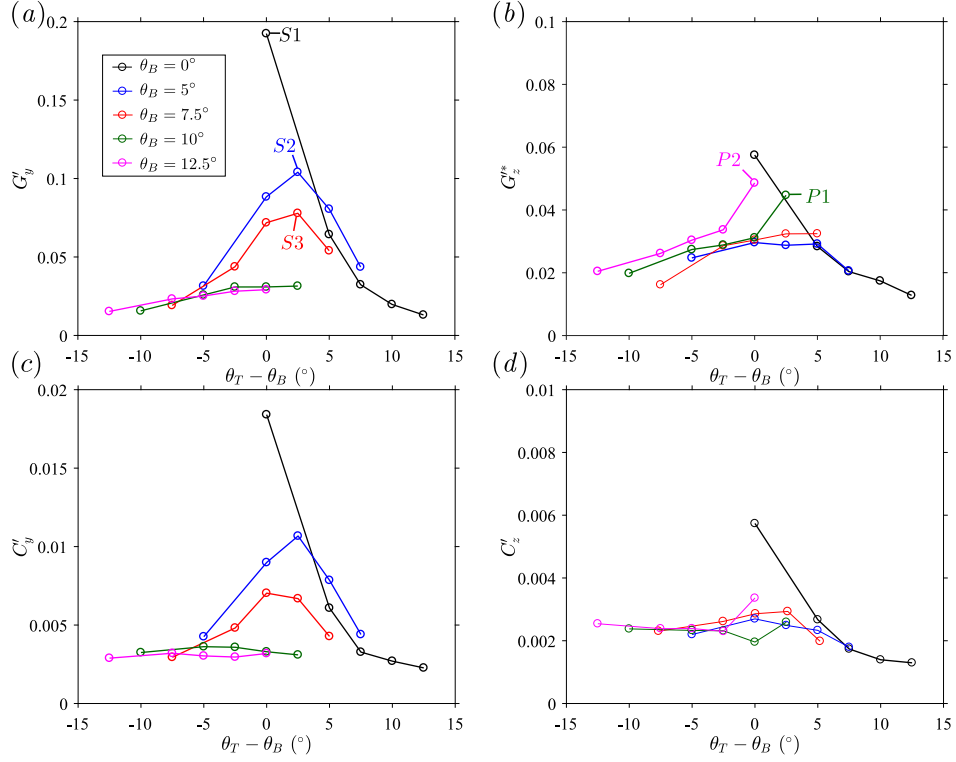
11

Figure 3: Mean fluctuations of the y-component (a, c) and z-component (b, d) of the base pressure gradient (a, b) and force coefficient (c, d) vs. $\theta_T - \theta_B$.

2013b; Bonnavion et al., 2017) with an exponent close to -1.25 in the power spectral density of the y-component in figure $4(d)$. The energy extinction at low frequency that results from the stabilization is accompanied by the growth of a sharp peak at $\mathrm{St} = 0.25$ for the z-component as the angle of boat-tailing is increased from $S2$ to $S3$ in figure $4(e)$. However, this peak was hardly distinguishable for the square-back geometry $S1$. It is ascribed to a periodic vortex shedding resulting from the global Kármán instability as characterized in Grandemange et al. (2013b) for square-back geometry. It involves the top and bottom separated shear layers since the oscillations

occur in the z-direction and only the vertical gradient is impacted (figure 3 and 5). We should mention that the large fluctuations in the z-component observed in figures 3(b, d) for the square-back configuration $S1$ are actually exclusively due to the long-time bi-stable dynamics – wake reversals – as shown by the large energy in the corresponding power spectral density in figure 4(e).

The pressure gradient time series for the two high fluctuating cases $P1$ and $P2$ are respectively shown in figures 5(a, b). Contrary to cases $S1$, $S2$ and $S3$, the amplitudes of the fluctuations in the z-direction are now larger that those in the y-direction, and their corresponding spectra exhibit a clear peak at approximately St $= 0.19$ in figure 5(d). In the y-direction, the spectra are flat in the low frequency range indicating the total absence of the long-time bi-stable dynamics (Grandemange et al., 2013b).

To summarize, while increasing the angles of the boat-tailing, the global y-instability of the wake (a three-dimensional instability) evidenced through the bi-stable dynamics of the specific configuration $S1$, $S2$ and $S3$ extinguishes. Meanwhile, the Kármán instability (a two-dimensional instability) develops. In the following section § 3.2, we study the adaptation of the wake asymmetry orientation as well as the asymmetry strength to changes of angles of the boat-tailing. The asymmetry strength is characterized through the magnitude g_r^* and the orientation through the phase angle φ of the base pressure gradient.

3.2.   Wake asymmetry and boat-tailing

The pressure gradient is expressed in the polar form (g_r^*, φ) and studied through the statistics of both coordinates. We will look at the evolutions
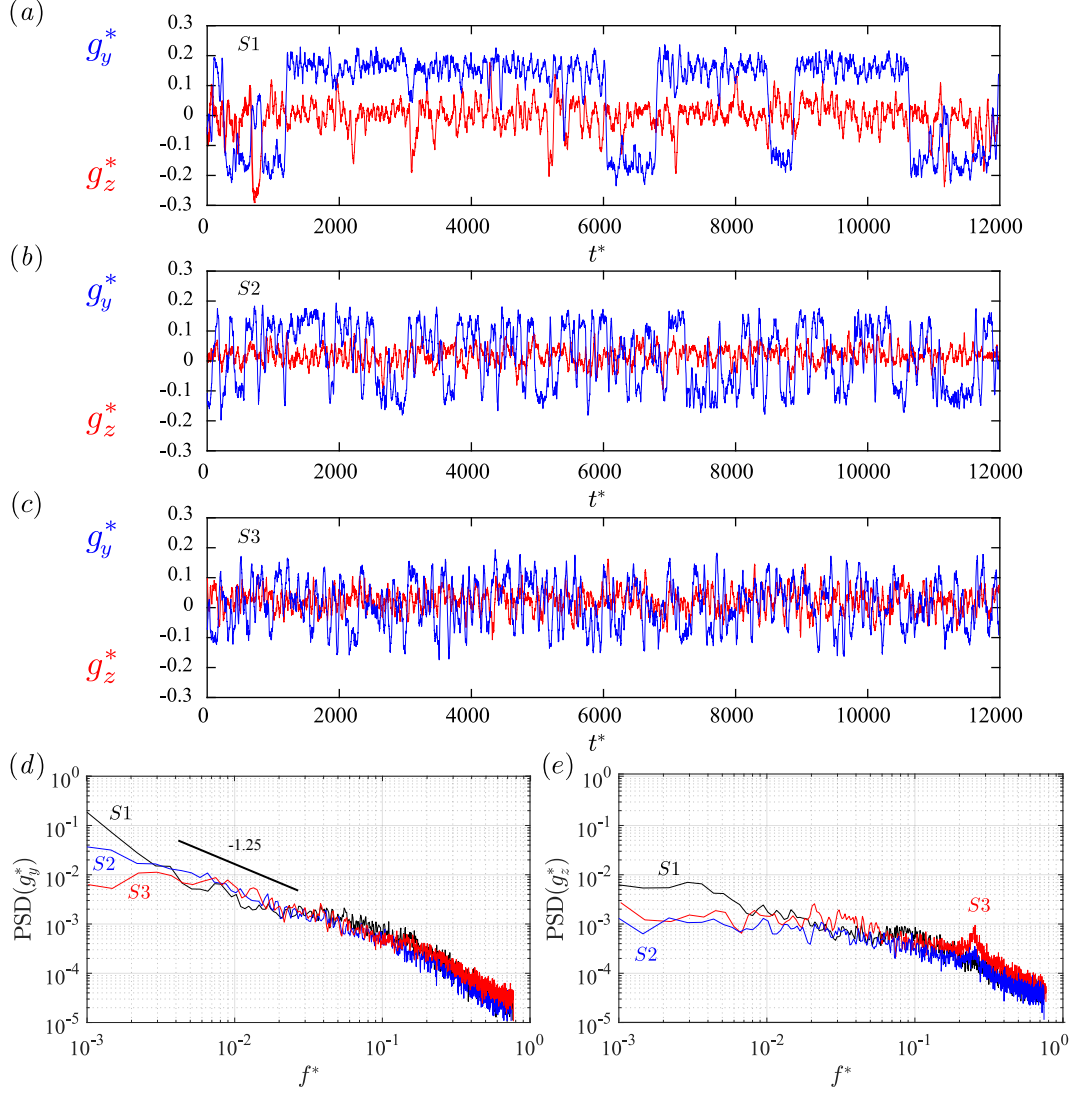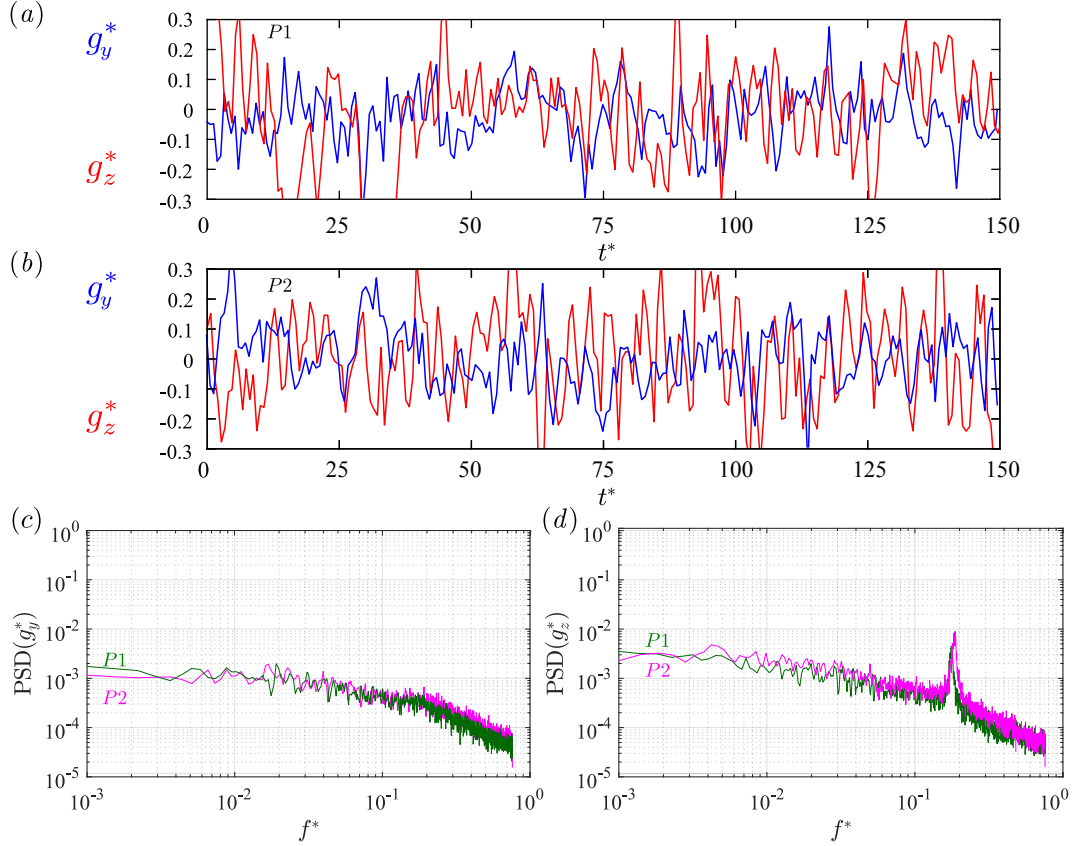
Figure 4: (a, b, c): time series of the base pressure gradient components $g_y^*(t)$ and $g_z^*(t)$ for the configurations $S1$ (a), $S2$ (b), and $S3$ (c). Corresponding power spectra of the g_y^* (d) and g_z^* (e) component. Time series in (a, b, c) have been low pass filtered ($f_c^* = 0.03$) to emphasize the long-time bistable dynamics

of these statistics for a fixed bottom angle θ_B varying the top angle θ_T as we did in figures 2 and 3. First, we consider the configurations with $\theta_B = 0°$

14

Figure 5: (a, b): time series of the base pressure gradient components $g_y^*(t)$ and $g_y^*(t)$ for the configurations $P1$ (a), $P2$ (b). Corresponding power spectra of the (c) g_y^* and (d) g_z^* component.

whose results are displayed in figures $6(a, b)$. In figure $6(a)$ we can see that the smallest non-zero top angle has a straightforward effect to lock the orientation of the base pressure gradient at $\varphi = -\pi/2$, while it was initially bi-stable between the two opposite orientations $\varphi = 0$ and $\varphi = \pi$ for the square-back after-body (*i.e.* configuration $S1$). This global wake rotation from horizontal at $\theta_T = 0°$ to vertical pressure gradient at $\theta_T = 5°$ is accompanied by a strong reduction by a factor 2 of the gradient magnitude (figure $6b$). As the top angle

15

is further increased, the vertical negative orientation of the gradient remains, while the magnitude continuously decreases as already reported above from figure 2(b).

In figures 6(c, d), a different scenario is obtained for the configurations with $\theta_B = 5°$. The statistics of the bi-stable configuration $\theta_T = 7.5°$ (i.e. configuration $S2$) displaying an almost equal exploration of the opposite orientations $\varphi = 0$ and $\varphi = \pi$ in figure 6(c) still remains bi-stable when the top angle is either increased to $\theta_T = 10°$ or reduced to $\theta_T = 5°$. However each bi-stable dynamics involves approximately either the two orientations $\varphi = \pi/4$ and $\varphi = 3\pi/4$ for $\theta_T = 5°$ or the two opposite ones $\varphi = -\pi/4$ and $\varphi = -3\pi/4$ for $\theta_T = 10°$. Eventually for both extreme values $\theta_T = 0°$ and $\theta_T = 12.5°$, the phase locks to give a permanent positive (i.e. $\varphi = \pi/2$) or negative (i.e. $\varphi = -\pi/2$) vertical pressure gradient. During this global rotation, the asymmetry given by the gradient modulus in figure 6(d) remains remarkably constant. This scenario is very similar to that observed by Barros et al. (2017) obtained by disturbing the underbody flow with varying cylinder sizes and Bonnavion and Cadot (2018) by changing the pitch of the y-unstable square-back Ahmed body. We consequently retrieve the adaptation mechanism of the y-instability proposed by Bonnavion and Cadot (2018): the boat-tail imposes a gradient component in the minor direction of the rectangular base (i.e. the z-direction) on which the gradient orientates to keep its modulus constant, equal to the strength of the y-instability.

The two other series with fixed bottom angles at $\theta_B = 10°$ and $12.5°$ that lead to the periodic mode are shown in figure 7. The Kármán instability dominates for the two larger top angles $10°$ and $12.5°$ as indicated by the
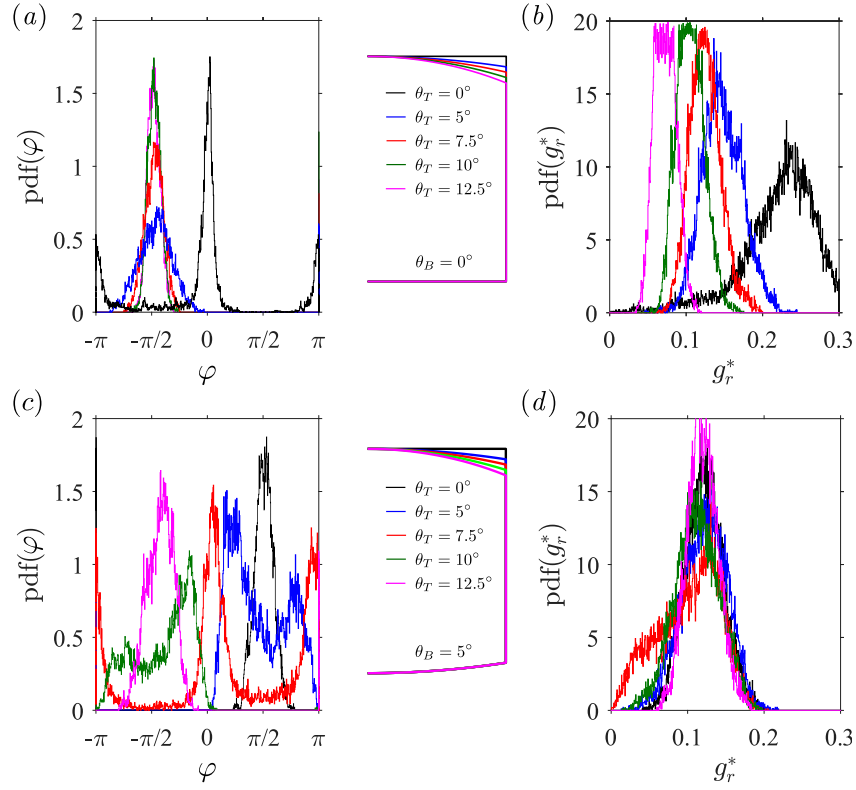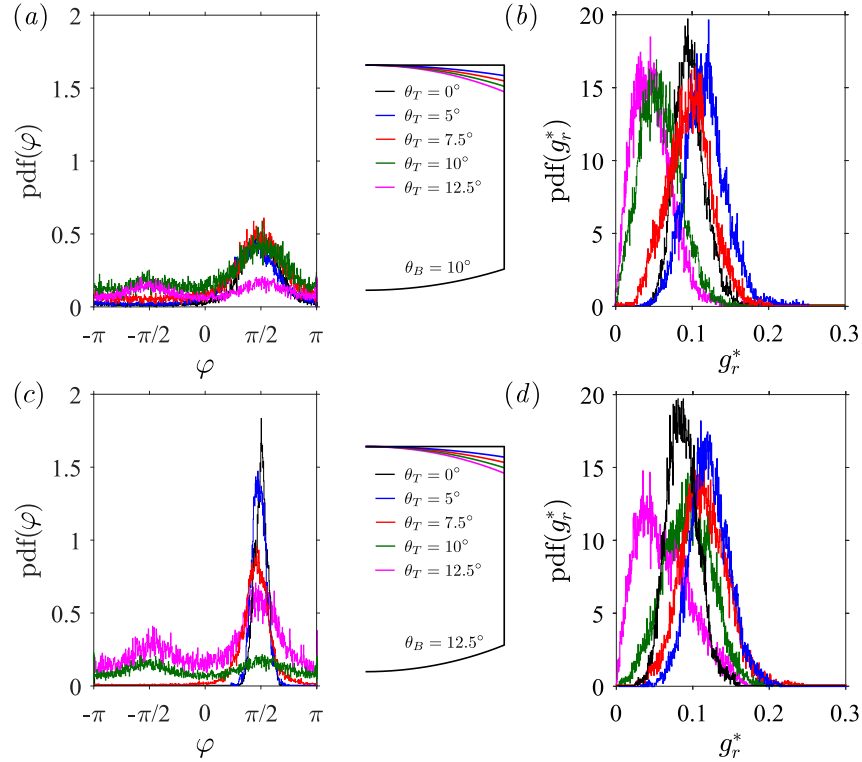
Figure 6: Probability density functions of phase φ (a, c) and modulus g_r^* (b, d) of the pressure gradient varying the top angle θ_T for fixed bottom angles $\theta_B = 0°$ (a, b) and $\theta_B = 5°$ (c, d) with. Afterbody geometries are illustrated.

appearance of two most probable orientations at $\varphi = \pm\pi/2$ in figures $7(a, c)$. It is accompanied by a strong attenuation of the gradient modulus in figures $7(b, d)$ with a most probable value approximately reduced to 0.05 while, except for one case at $(\theta_B = 0°, \theta_T = 12.5°)$ in figure $6(b)$, the modulus is always around or above 0.1 for all investigated boat-tails.

Figure 7: Probability density functions of phase φ (a, c) and modulus g_r^* (b, d) of the pressure gradient varying the top angle θ_T for fixed bottom angles $\theta_B = 10°$ (a, b) and $\theta_B = 12.5°$ (c, d) with. Afterbody geometries are illustrated

3.3. Drag

We finally address the consequence of the boat-tailing on the mean base suction and drag coefficients C_b and C_x. The drag coefficient of the 25 configurations is plotted in figure 8(a) against the difference between the top and bottom boat-tail angles $\theta_T - \theta_B$. It essentially shows that increasing the boat-tailing angles with $\theta_T - \theta_B \approx 0°$ from $\theta_B = 5°$ up to $\theta_B = 12.5°$ is detrimental for drag. On the contrary, it is always beneficial for the mean base suction coefficient C_b defined in equation (2) and plotted in figure 8(b).

18

This classical effect was already evidenced in previous works of Mair (1969) and Wong and Mair (1983). The discrepancy is related to the drag on the boat-tail that can be either increased by the low pressures created by both the curvature and the development of longitudinal vortices at the four base corners or decreased by the diffuser shape of the boat-tail.
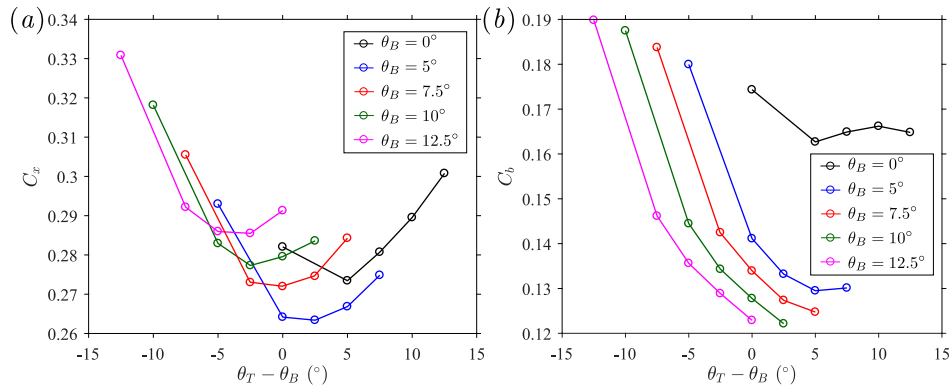

Figure 8: Influence of boat-tails angles on (a) the mean drag coefficient C_x and (b) the mean base suction coefficient C_b.

We can see in figure 8(a) that the lowest drag is achieved for the configuration $S2$ ($\theta_B = 5°$, $\theta_T - \theta_B = 2.5°$) that is one of the most fluctuating cases subject to the y-instability as studied above. The reduction is about 6.7% compared to the baseline. As shown by Grandemange et al. (2015), further drag reduction of a few percent can be obtained by removing the y-instability from this optimal boat-tail. On the other hand, the maximum drag increase is measured to be +15% when only one large boat-tail is in place.

4. Discussion

Compared to the square-back geometry, the application of a single, either top or bottom, chamfer of 5° reduces the permanent wake asymmetry by a

factor two. Bi-stable dynamics are still observable for similar top and bottom angles creating high global fluctuations in the wake, in agreement with previous observations of Perry et al. (2016) about the Windsor body. Different top and bottom angles produce a vertical pressure gradient on which the asymmetric wake adapts accordingly to the mechanism proposed by Bonnavion and Cadot (2018).

A transition between the two wake regimes, namely the wake subject to the y-instability and the Kármán periodic wake mode, is identified in § 3.1. In order to investigate whether the flow orientation at separation is responsible for the transition, we compare two boat-tailing having same angles at separation chosen as $\theta_T = \theta_B = 12.5°$, but with different boat-tail length. The dynamics of the wake orientation given by the phase φ of the pressure gradient is used as the global instability type indicator. The phase spectrum obtained with the boat-tail used above (configuration $P2$) is shown in figure $9(a)$ as the red curve. As already noticed in figure $5(d)$, the periodic mode is present as indicated by the peak and the energy distribution at low frequencies is flat. The second new configuration with identical angles was produced with a shorter boat-tail having $\ell = 0.168\ H$. The corresponding phase spectrum shows a power law distribution at very low frequencies, produced by the bi-stable dynamics while no peak associated with a periodic mode is observable. The global wake dynamics is then dominated by the y-instability for the short boat-tail and by the Kármán periodic mode for the long one. The only similar transition observation in other works, is to our knowledge the stability analysis of Marquet and Larsson (2014) of a flat plate facing a uniform flow at low Reynolds number. A transition between steady

20

symmetry breaking modes (equivalent to static asymmetries for the turbulent wake) and periodic antisymmetric modes is observed changing the plate aspect ratio. Large aspect ratios render the geometry more two-dimensional which are favourable to the periodic antisymmetric modes while aspect ratio of order 1 are more likely to trigger steady three-dimensional instabilities. In the case of the figure 9(a), the short boat-tail presents an aspect ratio of $\kappa = 1.269$ while with long boat-tails, the aspect ratio is increased to $\kappa = 1.541$.

To generalize to all investigated aspect ratios, figure 9(b) shows the strength of the permanent asymmetry as the average of the modulus of the base pressure gradient $\overline{g_r^*}$. It is plotted versus the aspect ratio $\kappa = W/H_B$ of the vertical base (as defined in figure 1) and the boat-tail angles difference $\theta_T - \theta_B$. We believe that the wake is not subject to the static y-instability for $\overline{g_r^*} < 0.06$. For the largest base aspect ratios, it is suggested that the static instability is stabilized, possibly following a similar scenario as that evidenced by Marquet and Larsson (2014) leading to a wake dominated by the global Kármán instability.

5. Conclusion

Our work shows that, within the limitation of the aspect ratio of the base, the y-instability persists and dominates the wake dynamics. As boat-tails are installed at the after-body, they generate a base pressure gradient component along the minor axis of the rectangular base (i.e. the vertical direction $\mathbf{e_z}$) on which the instability adapts following the mechanism proposed by Bonnavion and Cadot (2018). As a result, different wake dynamics and orientations are
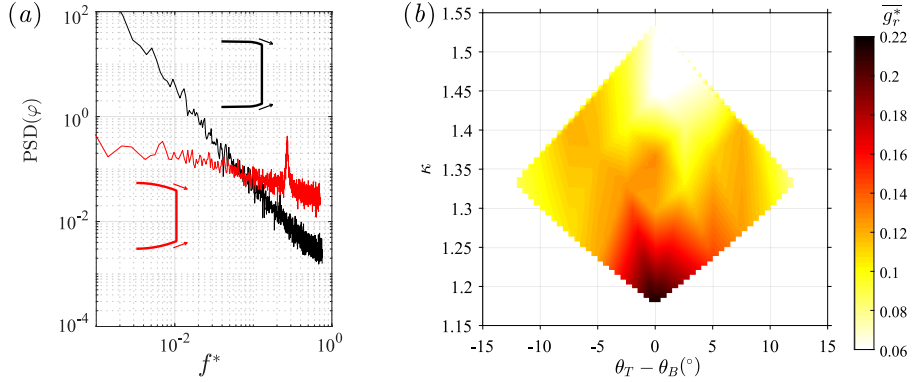
Figure 9: (a) Power spectra of the phase φ of the base pressure gradient for two boat-tails having different vertical base aspect ratio, $\kappa = 1.541$ (in red) and $\kappa = 1.269$ (in black) but identical angles at separation $\theta_T = \theta_B = 12.5°$. (b) Mean value of the modulus of the base pressure gradient $\overline{g_r^*}$ plotted against the difference between the top and bottom boat-tail angles $\theta_T - \theta_B$ and the base aspect ratio κ defined in § 2.

obtained. This characteristic can be used as an additional control on the lift exerted on the body. For bi-stable configurations, the switching frequency is found to increase with larger angles. For unpropitious aspect ratios, the static instability yields to a periodic wake mode related to vortex-shedding, with vertical fluctuations of the wake. The drag of the vehicle is found to result from two opposite mechanisms: a base pressure recovery associated with a diffuser effect and the low-pressure generated drag on the boat-tails related to their curvature. Finally, it is found that the periodic mode should be avoided in the seek of drag reduction and that the best results are obtained for y-unstable configurations with almost equal angles, *i.e.* when the bi-stable dynamics is present. Following this work, it would be of highest interest to study the effect of the top and bottom boat-tail for a body subject to the

22

z-instability, since it corresponds to the situation generally observed on real minivans (Bonnavion et al., 2017, 2019). The difference with the y-instability is only the static asymmetric states orientation that is in the vertical direction for the z-instability while it is in the horizontal one for the y-instability. A full characterisation of the global z-instability of the turbulent wake can be found in Grandemange et al. (2013a); Schmidt et al. (2018); Bonnavion and Cadot (2018).

Acknowledgments

References

Barros, D., Borée, J., Cadot, O., Spohn, A., Noack, B.R., 2017. Forcing symmetry exchanges and flow reversals in turbulent wakes. Journal of Fluid Mechanics 829, R1.

Bonnavion, G., Cadot, O., 2018. Unstable wake dynamics of rectangular flat-backed bluff bodies with inclination and ground proximity. Journal of Fluid Mechanics 854, 196–232.

Bonnavion, G., Cadot, O., Évrard, A., Herbert, V., Parpais, S., Vigneron, R., Délery, J., 2017. On multistabilities of real car's wake. Journal of Wind Engineering and Industrial Aerodynamics 164, 22–33.

Bonnavion, G., Cadot, O., Herbert, V., Parpais, S., Vigneron, R., Délery, J., 2019. Asymmetry and global instability of real minivans' wake. Journal of Wind Engineering and Industrial Aerodynamics 184, 77–89.

Evrard, A., Cadot, O., Herbert, V., Ricot, D., Vigneron, R., Délery, J., 2016. Fluid force and symmetry breaking modes of a 3D bluff body with a base cavity. Journal of Fluids and Structures 61, 99–114.

Evstafyeva, O., Morgans, A.S., Dalla Longa, L., 2017. Simulation and feedback control of the Ahmed body flow exhibiting symmetry breaking behaviour. Journal of Fluid Mechanics 817, R2.

Grandemange, M., Cadot, O., Courbois, A., Herbert, V., Ricot, D., Ruiz, T., Vigneron, R., 2015. A study of wake effects on the drag of the Ahmed squareback model at the industrial scale. Journal of Wind Engineering and Industrial Aerodynamics 145, 282–291.

Grandemange, M., Gohlke, M., Cadot, O., 2012. Reflectional symmetry breaking of the separated flow over three-dimensional bluff bodies. Physical Review E 86, 035302.

Grandemange, M., Gohlke, M., Cadot, O., 2013a. Bi-stability in the turbulent wake past parallelepiped bodies with various aspect ratios and wall effects. Physics of Fluids 25, 95–103.

Grandemange, M., Gohlke, M., Cadot, O., 2013b. Turbulent wake past a three-dimensional blunt body. Part 1. Global modes and bi-stability. Journal of Fluid Mechanics 722, 51–84.

Grandemange, M., Gohlke, M., Cadot, O., 2014. Turbulent wake past a three-dimensional blunt body. Part 2. Experimental sensitivity analysis. Journal of Fluid Mechanics 752, 439–461.

Grandemange, M., Mary, A., Gohlke, M., Cadot, O., 2013c. Effect on drag of the flow orientation at the base separation of a simplified blunt road vehicle. Experiments in fluids 54, 1–10.

Han, T., Hammond, D., Sagi, C., 1992. Optimization of bluff body for minimum drag in ground proximity. AIAA Journal 30, 882–889.

Littlewood, R., Passmore, M., 2010. The optimization of roof trailing edge geometry of a simple squareback. SAE Technical Paper Series 2010-01-0510.

Mair, W.A., 1969. Reduction of base drag by boat-tailed afterbodies in low-speed flow. Aeronautical Quarterly 20, 307320.

Marquet, O., Larsson, M., 2014. Global wake instabilities of low aspect-ratio flat-plates. European Journal of Mechanics B/Fluids 49, 400–412.

Pavia, G., Passmore, M., Gaylard, A., 2016. Influence of short rear end tapers on the unsteady base pressure of a simplified ground vehicle. SAE Technical Paper Series 2016-01-1590.

Perry, A., Pavia, G., Passmore, M., 2016. Influence of short rear end tapers on the wake of a simplified square-back vehicle: wake topology and rear drag. Experiments in Fluids 57, 169.

Roshko, A., 1993. Perspectives on bluff body aerodynamics. Journal of Wind Engineering and Industrial Aerodynamics 49, 79–100.

Schmidt, H.J., Woszidlo, R., Nayeri, C.N., Paschereit, C.O., 2018. The effect of flow control on the wake dynamics of a rectangular bluff body in ground proximity. Experiments in Fluids 59, 107.

Volpe, R., Devinant, P., Kourta, A., 2015. Experimental characterization of the unsteady natural wake of the full-scale square back Ahmed body: flow bi-stability and spectral analysis. Experiments in Fluids 56, 99.

Wong, D.M., Mair, W., 1983. Boat-tailed afterbodies of square section as drag-reduction devices. Journal of Wind Engineering and Industrial Aerodynamics 12, 229 – 235.